We are IntechOpen, the world's leading publisher of Open Access books Built by scientists, for scientists

4,800
Open access books available

122,000
International authors and editors

135M
Downloads

Our authors are among the

154
Countries delivered to

TOP 1%
most cited scientists

12.2%
Contributors from top 500 universities

WEB OF SCIENCE™

Selection of our books indexed in the Book Citation Index in Web of Science™ Core Collection (BKCI)

Interested in publishing with us?
Contact book.department@intechopen.com

Numbers displayed above are based on latest data collected.
For more information visit www.intechopen.com

Chapter 5

Perovskite Oxide Nanocrystals — Synthesis, Characterization, Functionalization, and Novel Applications

Heng Wu and Xinhua Zhu

Additional information is available at the end of the chapter

http://dx.doi.org/10.5772/61640

Abstract

Perovskite oxide nanocrystals exhibit a wide spectrum of attractive properties such as ferroelectricity, piezoelectricity, dielectricity, ferromagnetism, magnetoresistance, and multiferroics. These properties are indispensable for applications in ferroelectric random access memories, multilayer ceramic capacitors, transducers, sensors and actuators, magnetic random access memories, and the potential new types of multiple-state memories and spintronic devices controlled by electric and magnetic fields. In the past two decades, much effort has been made to synthesize and characterize the perovskite oxide nanocrystals. Various physical and chemical deposition techniques and growth mechanisms are explored and developed to control the morphology, identical shape, uniform size, perfect crystalline structure, defects, and homogenous stoichiometry of the perovskite oxide nanocrystals. This chapter provides a comprehensive review of the state-of-the-art research activities that focus on the rational synthesis, structural characterization, functionalization, and unique applications of perovskite oxide nanocrystals in nanoelectronics. It begins with the rational synthesis of perovskite oxide nanocrystals, and then summarizes their structural characterizations. Fundamental physical properties of perovskite oxide nanocrystals are also highlighted, and a range of novel applications in nanoelectronics, information storages, and spintronics are discussed. Finally, we conclude this review with some perspectives/outlook and future researches in these fields.

Keywords: Perovskite oxide nanocrystals, synthesis, structural characterization, functionalization, applications

1. Introduction

Perovskite oxide nanocrystals have important properties in ferroelectricity, piezoelectricity, dielectricity, ferromagnetism, magnetoresistance, and multiferroics. The perovskite structure is named for the prototype $CaTiO_3$ mineral called perovskite, which is generally a metal oxide with the formula ABO_3, where B is a small transition metal cation and A is a larger s-, d-, or f-block cation. In a cubic perovskite, the larger cation A resides on the corners of the unit cell, the smaller cation B is in the center of the unit cell, and the oxygen ions (O_2^-) are on the centers of the faces [1]. The perovskite structure can also be built from three-dimensional corner-sharing BO_6 octahedra that are connected through B–O–B linkages. The A-site cation fits in the large cavity at the center of eight corner-sharing BO_6 octahedra, and the B-site cation resides in the interstitial site of an octahedron of oxygen anions [1]. Interestingly, and of technological importance, a variety of crystallize in the perovskite structure. Typical perovskite materials of technological importance are ferroelectric $BaTiO_3$, $PbTiO_3$, dielectric $(Ba,Sr)TiO_3$, piezoelectric $Pb(Zr,Ti)O_3$, electrostrictive $Pb(Mg,Nb)O_3$, magnetoresistant $(La,Ca)MnO_3$, and multiferroic $BiFeO_3$. They have attracted interest for several decades, with tremendous applications including ferroelectric random access memories, multilayer ceramic capacitors, transducers, sensors and actuators, magnetic random access memories, and the potential new types of multiple-state memories and spintronic devices controlled by electric and magnetic fields [1–8]. The major challenge in manufacturing these materials is the processing of the materials with reliable and reproducible properties [9, 10]. Following a similar trend to the miniaturization as the conventional CMOS (complementary metal oxide semiconductor) devices, the down-sized electronic devices based on perovskite electronic ceramic materials have also been developed. Advances toward nanoscale electronics have additionally increased interest in this field of perovskite oxide nanocrystals [11–13]. For example, to develop high volume efficient multilayered ceramic capacitors (MLCCs), the sizes of $BaTiO_3$ nanoparticles with high purity and uniform shape used for fabricating the next generation of MLCCs will be lowered down to tens of nanometers. Therefore, synthesis of high-purity, ultra-fine, and agglomerate-free perovskite nanoparticles with controlled particle size, morphology, and stoichiometry is the critical step in processing of perovskite ceramics with desirable properties. Perovskite oxide nanocrystals with the general formula of ABO_3 play a very important role in today's technological advances, which can be found in the application fields of passive dielectric materials, piezoelectric actuators and transducers, sensors, and micro/nano electromechanical systems and many more.

The evolution of a method to produce perovskite oxide nanocrystals with precise stoichiometry and desired properties is much complex. Conventionally, perovskite nanoparicles are prepared by solid-state reactions between the corresponding oxides or oxides and carbonates at temperatures above 1000°C [14, 15]. However, the resulting microstructures of perovskite nanoparticles obtained from this method are not suitable for the miniaturization of electronic devices, due to their significant particle agglomeration, poor chemical homogeneity, and coarse large particle sizes. To resolve the problems arising from the conventional ceramic techniques and to produce homogeneous and stoichiometric perovskite nanocrystals, in recent years, wet chemical routes have been developed [12, 16–18]. They can be better controlled from

http://dx.doi.org/10.5772/61640

the molecular precursor to the final material to give highly pure and homogeneous products, allowing for the low reaction temperatures used. The size and morphology of the nanocrystals can be controlled, and metastable phases could be prepared [18].

The objective of this chapter is to provide an overview of the state-of-the-art in perovskite nanocrystals, which covers their synthesis, characterization, functionalization, and novel applications. First, we review the synthetic methods for perovskite nanocrystals, which include the syntheses using solid and liquid precursors. The second section deals with the electron microstructural characterization of perovskite nanocrystals. In the context of functionalization, we discuss the unique properties of perovskite oxide nanocrystals (e.g., ferroelectric and dielectric, electrical, magnetic, and multiferroic properties), and the size effects for these unique properties are also discussed. And then a broad range of novel applications of perovskite oxide nanocrystals is addressed. Finally, we provide a perspective on the future outlook of perovskite nanocrystals.

2. Synthesis of perovskite oxide nanocrystals

Due to the particle size, dimensionality, and composition governing the resultant properties of the nanostructured perovskite materials that are assembled from nanocrystals as building blocks to achieve certain desired properties, the synthesis of high-purity, ultra-fine, and agglomerate-free perovskite oxide nanocrystals with controlled particle size, morphology, and stoichiometry is the first and perhaps the most crucial step in processing of perovskite ceramics with desirable properties. The major issues for the synthesis of perovskite oxide nanocrystals include: (a) the control of particle size and composition and (b) the control of the interfaces and distributions of the nanobuilding blocks within the fully formed nanostructured perovskite compounds. Over the past several decades, various methods have been developed to prepared perovskite oxide nanocrystals and the related nanostructured perovskite compounds. In the subsequent sections, some important methods for the preparation of perovskite oxide nanocrystals are described.

2.1. Solid-state reaction method

The solid-state reaction method is the most traditional one for preparing perovskite oxide nanocrystals (e.g., $BaTiO_3$, $PbTiO_3$, $Pb(Zr,Ti)O_3$, etc.) [14, 15]. This process includes weighting starting materials (the corresponding oxides or oxides and carbonates), mixing, milling, and calcining them at elevated temperatures to form the perovskite phase. For example, in synthesis of $BaTiO_3$ nanocrystals by solid-state reaction method, the reaction process in air has been proposed to take place in at least three stages and relies on the diffusion of Ba^{2+} ions into TiO_2 [19]. Firstly, $BaCO_3$ reacts with the outer surface region of TiO_2 to form a surface layer of $BaTiO_3$ on individual TiO_2 grains. Further diffusion of Ba^{2+} ions into TiO_2 necessitates the formation of Ba_2TiO_4 between the unreacted $BaCO_3$ and the previously formed $BaTiO_3$. After prolonged sintering periods, the intermediate Ba-rich phase Ba_2TiO_4 reacts with the remaining TiO_2 in the core-regions of the TiO_2 grains to form $BaTiO_3$. The high-temperature calcination

produces an agglomerated powder with a coarse particle size which requires additional milling process. However, contamination and other undesirable features during the milling process can create defects in the manufactured products. Furthermore, the more components in the ceramic powders, the more difficult it may be to achieve the desired homogeneity, stoichiometry, and phases. By using nanocrystalline $BaCO_3$ and TiO_2 as starting materials, Buscaglia et al. [20] have recently synthesized the perovskite $BaTiO_3$ nanocrystals with size of ~100 nm and narrow particle size distribution, *via* a solid-state reaction at calcination temperatures as low as 800°C. The average particle size of powders obtained *via* this method is essentially determined by the particle size of the used TiO_2 because the reaction rate is controlled by the diffusion rate of barium ions into the TiO_2 lattice [21]. Similar reaction mechanism was also found in the synthesized process of $BaZrO_3$ powders [22]. The morphology of $BaZrO_3$ nanoparticles was dependent upon the initial size and shape of the used starting ZrO_2 particles. Therefore, fine $BaZrO_3$ powders with particle size of 70–100 nm composing of crystallites of ~ 20–30 nm can be synthesized by using very fine (70–90 nm) starting ZrO_2 particles and coarse (~ 1 μm) $BaCO_3$ particles commercially available and calcination at ~1000°C. Higher calcination temperatures accelerate the initial stage of reaction but often lead to coarser and more-agglomerated powders.

2.2. Molten-Salt Method (MSS)

Molten-salt synthesis (MSS) is one of the methods for preparing perovskite oxide nanopowders, which involves the use of a molten salt as the medium for preparing perovskite oxides from their constituent materials (oxides and carbonates) [23]. This method allows melt-solid reacting much faster due to the small diffusion distances and higher mobility of oxides in the melt. Many molten salt solvents such as alkali chlorides, sulphates, carbonates, and hydroxides are used in the past acting as a medium of reaction for the constituent oxides. MSS attracted much attention due to its advantages such as one-step, rapid, and environmentally friendly for synthesizing perovskite oxide functional materials. The melt increases the reaction rate due to the small diffusion distances and high mobility of oxides in it. In addition, as a medium of the reaction, the choice of the molten salt system is variety, e.g., alkali chlorides, sulphates, carbonates, and hydroxides. The features of this synthetic method are the simplest, versatile, and cost-effective approaches available for obtaining a pure perovskite phase at a relatively low temperature for a shorter soaking time. Generally, the procedure of synthesize perovskite oxide powders by MSS is shown below. First, heating the raw materials consisting of reactants and salt system above the melting temperature of the salt, so that the produced particles are synthesized at the melted salt solvent. The characteristics of the powders can be controlled by tuning the heating temperature and duration time. After cooling down to room temperature naturally, the product is washed by appropriate solvent (typically, deionized water) and dried subsequently, and the complex perovskite oxide powder is obtained. In the past decade, MSS has been widely used to synthesize a range of perovskite oxide nanocrystals. For example, perovskite $SrFeO_3$ nanocrystals were successfully synthesized in molten $NaNO_3$–KNO_3 eutectic with Na_2O_2 from a mixture of strontium nitrate and ferric nitrate [24]. The effects of metal precursors, salt medium, annealing temperature, and oxidizing properties of the melt on the phase compositions, crystallite sizes, and morphology of the resulting metal oxides were

http://dx.doi.org/10.5772/61640

systematically investigated. It was found that the formation of the $SrFeO_3$ phase was mainly dependent upon the nature of the metal precursor and salt medium. Metal nitrates were the suitable precursors and $NaNO_3$–KNO_3 eutectic with Na_2O_2 was the suitable salt medium, which resulted in the formation of pure $SrFeO_3$ nanocrystals at a much lower temperature of 400°C. Pure cubic phase $SrTiO_3$ nanocrystals were synthesized in the eutectic NaCl–KCl molten salts at 700°C by heating TiO_2 and $Sr(NO_3)_2$ powders for 6 h [25]. The sizes of the as-synthesized $SrTiO_3$ nanocrystals were dependent upon the kinds of TiO_2 precursors, indicating that the formation process of $SrTiO_3$ in the molten salts was mainly controlled by the template formation mechanism. Single-crystalline perovskite $BaZrO_3$ nanocrystals were also obtained using BaC_2O_4 and ZrO_2 as precursors and NaOH/KOH as the molten salts at 700°C [26]. Rare earth orthoferrites with the general formula of $LnFeO_3$ (Ln = La, Pr, Nd) were synthesized in molten NaOH flux at 400°C [27], and $LaMO_3$ (M = Mn, Fe, Co, Ni) were obtained in molten nitrates or nitrites [28]. Recently, perovskite Pb-based relaxors [29], Ba-based dielectric oxides [30], and perovskite multiferroic bismuth ferrites [31–35] were also synthesized by MSS process.

2.3. Wet chemical methods

Since perovskite oxide nanocrystals synthesized *via* conventional solid-state reactions have uncontrolled and irregular morphologies, the electrical properties of the sintered ceramics are very poor. To solve this problem, various wet chemical methods have been developed to synthesize perovskite nanocrystals. The popular wet chemical methods for the preparation of perovskite nanocrystals, include sol–gel method [36–38], alkoxide–hydroxide sol-precipitation method [39–41], hydrothermal method [42–44], microwave-hydrothermal [45–47], and solvothermal syntheses [48–50]. The most important advantages of the wet chemical methods include easy controlling of the chemical stoichiometry, producing nanocrystals with narrow size distribution, and low crystallization temperature due to the constituents mixed at the quasi-atomic level in a solution system. Due to the wet chemical solution process, a dopant such as paramagnetic ions or rare-earth ions could be readily introduced during the preparation of the precursor solution. In the following subsequent sections, various wet chemical methods used for preparation of perovskite oxide nanocrystals are introduced.

2.3.1. Sol–gel (colloidal) processing

Sol–gel process is a popular processing route for the synthesis of perovskite oxide nanocrystals (e.g., $BaTiO_3$, $PbTiO_3$, $BiFeO_3$) [36–38]. This process involves the formation of a sol by dissolving the metal aloxide, metal-organic, or metal-inorganic salt precursors in a suitable solvent, subsequent drying of the gel followed by calcination and sintering at high temperature to form perovskite nanocrystals. Due to the reacting species homogenized at the atomic level in a sol–gel process, the diffusion distances are considerably reduced compared to a conventional solid-state reaction; therefore, the product can be formed at much lower temperatures. In this process, the selection of starting materials, concentration, pH value, and heat treatment schedule play an important role in affecting the properties of perovskite nanocrystals. This has been demonstrated in the case of $BaTiO_3$

perovskite oxide nanocrystals [38, 51, 52]. Barium acetate and titanium isopropoxide are often used as starting materials to synthesize $BaTiO_3$ nanocrystals. However, the different rates in the hydrolysis and condensation of Ba and Ti precursors often give rise to the chemical component segregation in the obtained gels. To solve this problem, acetic acid or acetylaceton was often used to control the hydrolysis rate of the Ti precursor, since these complexing agents acts as chelating agents to coordinate with Ti species [53,54].

For the obtained gels, a heat treatment at high temperature over 600°C is required to remove the unreacted organics and to crystallize the powders. Several steps involve in the transformation from the precursor to the crystalline $BaTiO_3$ nanocrystals, including the transformation from the precursor to the amorphous $BaTiO_3$, and then to the three-dimensional nucleation of the crystalline $BaTiO_3$ in the amorphous matrix, and finally to the nanocrystal growth of $BaTiO_3$ *via* a solid-state reaction [55]. To better control the grain size and its distribution, the heat treatment process parameters of the gels (e.g., post-annealing temperature, time and atmosphere, heating rate) must be optimized [56]. Normally, higher annealing temperature or longer annealing time can lead to larger grain size of the powders, while slow heating rate and inert annealing atmosphere can inhabit the aggregated behavior of nanocrystals in comparison to air or oxygen atmosphere. That was demonstrated in the synthesis of $Pb(Zr,Ti)O_3$ nanocrystals [56]. By using these techniques, monodispersed perovskite oxide nanocrystals and related nanostructured materials have been successfully fabricated. The particle size can be adjusted from a few nanometers to micrometers *via* controlling the solid-state polymerization and the heat treatment process [36, 55].

2.3.2. Hydrothermal process

Hydrothermal synthesis involves heating an aqueous suspension of insoluble salts in an autoclave at a moderate temperature and pressure where the crystallization of a desired phase is taking place. As a powerful method for synthesis of very fine and homogeneous perovskite powders with a controllable size distribution and morphology, its application to the growth of $BaTiO_3$ powders with the desired size and particle morphology has been widely investigated [57–60]. Based on the high-resolution transmission electron microscopy (HRTEM) observations on the incompletely and fully reacted powders, Pinceloup et al. [57] proposed a dissolution–precipitation model for hydrothermal synthesis of $BaTiO_3$ nanocrystals using $Ba(OH)_2$ and TiO_2 as precursors. In this model, TiO_2 particles are first dissolved to form hydroxyl titanium complexes $[Ti(OH)^{n-}]$ and then react with barium ions in the solution to precipitate $BaTiO_3$. On the other hand, Hertl [58] and Hu et al. [61] proposed another in situ heterogeneous transformation model, in which TiO_2 particles react initially with the dissolved barium to produce a continuous layer of $BaTiO_3$, and the additional barium must diffuse through this layer and reacts with TiO_2 until the supply of TiO_2 is exhausted. This model was supported experimentally by the hydrothermal conversion from TiO_2 microspheres to nanocrystalline $BaTiO_3$ [59]. Eckert et al. [60] also reported on a mechanism evolution from a dissolution–precipitation process at the early stage of the reaction to an in situ mechanism for the longer reaction times. Recently, Walton et al. [62] investigated the hydrothermal crystallization of $BaTiO_3$ by time-resolved powder neutron diffraction methods in situ, using the newly

http://dx.doi.org/10.5772/61640

developed Oxford/ISIS hydrothermal cell. They directly observed that the rapid dissolution of the barium source was followed by dissolution of the titanium source before the onset of crystallization of $BaTiO_3$. These qualitative observations strongly suggest that a homogeneous dissolution–precipitation mechanism dominates in the hydrothermal crystallization of $BaTiO_3$ rather than other possible mechanisms proposed in the literatures [81–83]. These contradictive experimental observations reported previously probably result from the different hydrothermal conditions.

2.3.3. Microwave-hydrothermal process

The microwave-hydrothermal process is a rapid process, which has the potential to enhance the crystallization kinetics of hydrothermal process. The term microwave-hydrothermal process was named by Komarneni et al. [63] in 1992, and this process has been used for the rapid synthesis of numerous ceramic oxides, hydroxylated phases, porous materials, and hematite powders [64–67]. It offers many distinct advantages over the conventional hydrothermal synthesis, such as cost savings, rapid internal heating, and synthesis of new materials.

Up to date, numerous reports have been published on the synthesis of $BaTiO_3$ nanocrystals by microwave-hydrothermal process below 200°C, and these processes were found to be very rapid but they all yielded cubic phase [45–47, 68]. For example, Khollam et al. [47] obtained submicron-sized $BaTiO_3$ powders (0.1–0.2 μm) at holding time of 30 min. One of the first approaches on the synthesis of the nanosized $BaTiO_3$ powders (about 30 nm) at 30 min was reported by Jhung et al. [69]. Recently, tetragonal $BaTiO_3$ powders are synthesized by microwave-hydrothermal method at a typical temperature of 240°C from hydrous titanium oxide and barium hydroxide, in the absence of chloride ions and alkali metal ions to avoid contaminations. The effects of synthesis conditions, including reaction temperature and time, and reactant composition, on the formation of tetragonal structure and particle size of $BaTiO_3$ powders, have been systematically investigated [70]. The results have shown that the amount of the tetragonal phase and the particle size increased quickly with reaction time, whereas the content of lattice hydroxyl groups decreased. Tetragonal $BaTiO_3$ powder with nearly full tetragonality (c/a ratio = 1.010) was obtained *via* the microwave-hydrothermal process performed at 240°C for 20 h [70]. As the reaction temperature was lowered down to 220°C, the formation of tetragonal structure and the growth of particles slowed down substantially, showing a critical effect of the reaction temperature on the microwave-hydrothermal processing of tetragonal $BaTiO_3$. Higher $Ba(OH)_2$/Ti mole ratio enhanced the formation of tetragonal $BaTiO_3$ and so did higher initial concentration of Ti with fixed $Ba(OH)_2$/Ti ratio. Besides the $BaTiO_3$ nanocrystals, $Ba_{1-x}Sr_xTiO_3$ (x = 0.1–0.4) nanocrystals with the average size about 20 nm were also prepared at a relatively short period of time (10 min) *via* microwave-hydrothermal synthesis [71]. The structure and the average size of BST were determined to be in the range of 20–50 nm depending on the synthesis time (10–90 min).

Perovskite $BiFeO_3$ nanocrystals exhibit multiferroic properties at room temperature (ferroelectric and magnetic order coexisting in the same phase) and is, therefore, a good candidate for potential multiferroic application in information technology. Recently, perovskite $BiFeO_3$ nanocrystals with diameters of 10–50 nm are synthesized by microwave-hydrothermal

synthesis [72,73]. The starting reactants are used as $Fe(NO_3)_3 \bullet 9H_2O$ and $Bi(NO_3)_3 \bullet 5H_2O$ together with KOH as the mineralizer. Figure 2 shows the XRD pattern of the perovskite $BiFeO_3$ nanocrystals synthesized by microwave-hydrothermal process. As shown in Figure 2, all the reflection peaks can be readily indexed as a rhombohedrally distorted perovskite BFO (JCPDS card No. 86-1518) with space group R3c and lattice parameters of a = 5.582 Å and c = 13.876 Å. No peaks from other phase were detected. In addition, the sharp diffraction peaks indicate that highly crystallized and phase-pure BFO nanocrystals can be obtained under the present synthesis conditions. The particle size and morphology of the as-obtained perovskite $BiFeO_3$ nanocrystals were revealed by TEM images. Figure 3(a) represents a typical low-magnitude TEM image, in which the BFO nanocrystals exhibit a spherical morphology with particle sizes of 15–55 nm. No agglomerated particles were observed, and nearly monodispersive behavior was observed in these BFO nanocrystals. Their statistic particle size distribution is shown in Figure 3(b), which clearly demonstrates that the average particle size of the BFO nanoparticle is ~35 nm, this value is much smaller than the previously reported ones [61, 74–77]. A high-magnification TEM image is shown in Figure 3(c), which clearly demonstrates the well-dispersed BFO nanocrystals with a spherical morphology. The selected area electron diffraction (SAED) pattern of the as-obtained BFO nanocrystals is shown in Figure 3(d), which exhibits polycrystalline diffraction rings consisting of discrete diffraction spots. Based on the analysis of the diffraction rings, the first six diffraction rings can be indexed as (012), (104)/(110), (006)/(202), (024), (116)/(122), and (214), which is in well agreement with the XRD results. The high crystallinity nature of the BFO nanocrystals is also proven by the lattice fringes observed in the HRTEM image. Figure 3(e) shows an HRTEM image taken from a single BFO nanocrystal with a particle size of ~12 nm, and the lattice fringes of (202) and (113) crystal planes are clearly resolved. The Fourier filtered HRTEM image of the single BFO nanocrystal is shown in Figure 3(f), and the inset is a fast Fourier transform (FFT) pattern of the nanocrystal obtained by Gatan Digital Micrography software. The angle between the (202) and (113) crystal planes measured from Figure 3(f) is 58°, which is very close to the theoretical value of 57.99° (the angle ∠(202):(113) = 57.99° for BFO). Therefore, the single-crystalline nature of BFO nanocrystals is confirmed by the SAED pattern and HRTEM image.

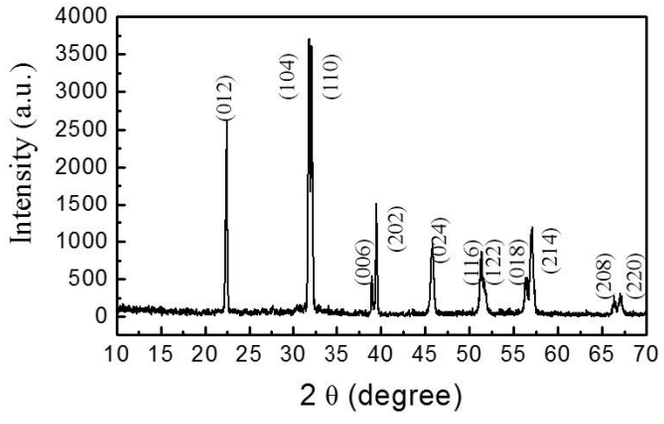

Figure 1. XRD pattern of the as-synthesized perovskite $BiFeO_3$ nanocrystals by microwave-hydrothermal reaction. Reproduced with permission from [73].

http://dx.doi.org/10.5772/61640

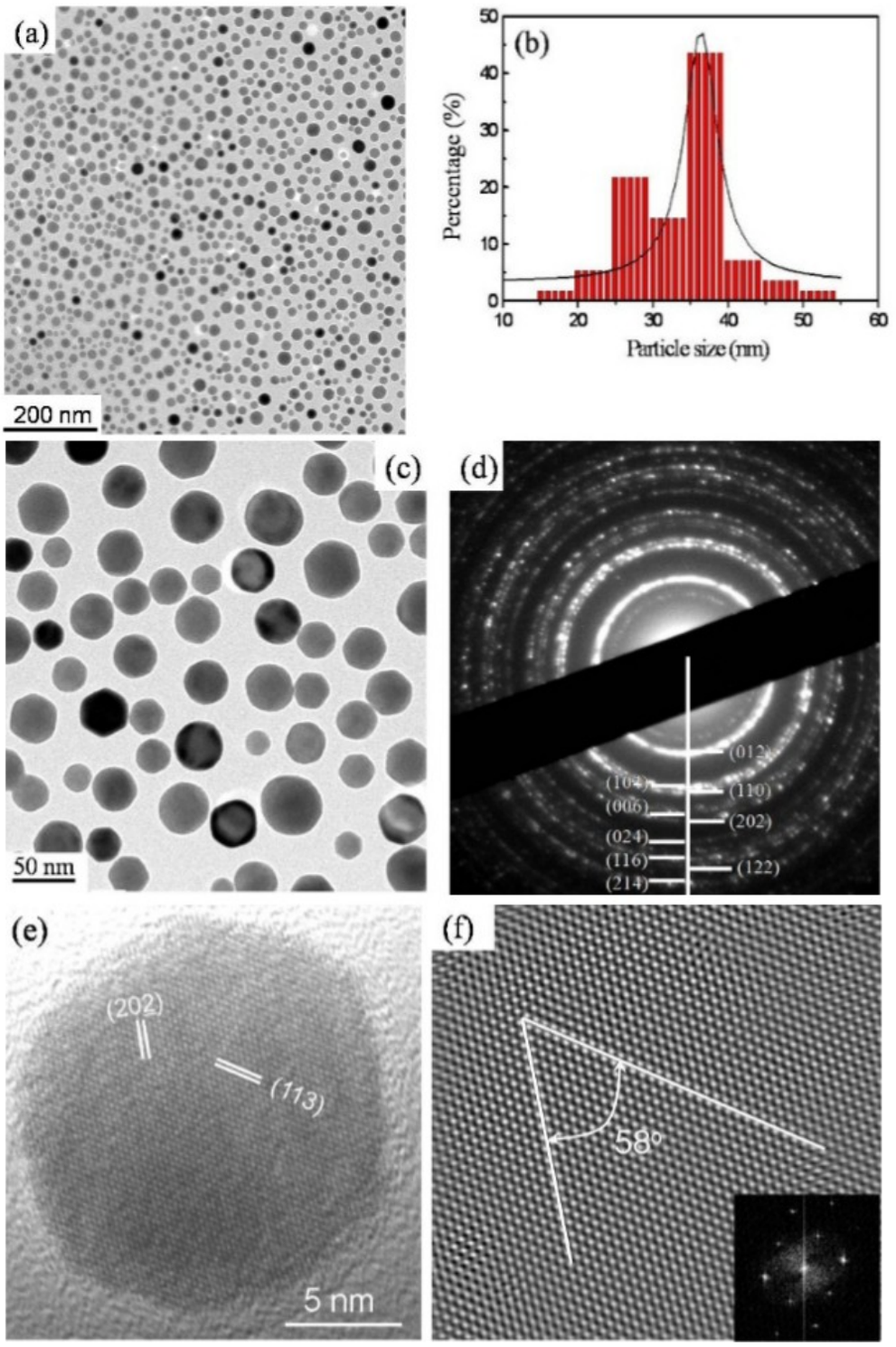

Figure 2. (a) Typical low-magnitude TEM image of the perovskite $BiFeO_3$ nanocrystals, (b) statistic particle size distribution obtained from low-magnitude TEM image, (c) high-magnitude TEM image, (d) selected area electron diffraction pattern, in which the first six diffraction rings are indexed as (012), (104)/(110), (006)/(202), (024), (116)/(122), and (214). (d) HRTEM image of a single perovskite BFO nanocrystal with a diameter of ~12 nm, and (e) Fourier filtered HRTEM image. Inset is a fast Fourier transform (FFT) pattern of the nanocrystal. Reproduced with permission from [73].

3. Structural characterization of perovskite oxide nanocrystals

Up to date, numerous TEM investigations have been carried out to investigate the microstructural features of perovskite $BaTiO_3$ nanocrystals [79–83]. For example, the internal pore structures in the hydrothermal $BaTiO_3$ nannopowders were examined by TEM [79]. Figure 3 shows TEM images of (a) as-received $BaTiO_3$ powder (particle size ~60 nm) and (b) $BaTiO_3$ powder annealed at 673 K. It was observed that some particles had internal pores of various sizes in as-received $BaTiO_3$ powders, as indicated by the arrows in Figure 3(a). A large pore with a cubic-shaped was observed in the particle annealed at 673 K in Figure 3(b). Lattice images were observed around the particle, and these indicated that the pore existed inside the particle. A three-dimensional structure of the internal pore was successfully observed and constructed by TEM tomography system. The results showed that no inclusion was found in the pores, and such internal pores were not lattice defects at the atomic level because their sizes were a few tens of nanometers. Large pores were involved in as-received $BaTiO_3$ powders, and their numbers decreased at >1,128 K. Some of the internal pores were released from the particle's surface and/or during the grain growth. The presence of the pores affected the density of the $BaTiO_3$ particle. The behavior of the internal pore was observed in situ with increasing temperature on the thermal stage of a TEM device. The results showed that at >1,128 K, some pores moved out from the particle's surface during TEM observation. This temperature roughly agreed with the temperature at which the density of $BaTiO_3$ powder sharply increases. During observation with increasing temperature, a thin layer appeared on the particle's surface at temperature over 573 K and then disappeared at 1,193 K.

The hydrothermal $BaTiO_3$ powder with a small particle size is stabilized in a cubic phase at room temperature [80–83], which implies that the distortion of the $[TiO_6]$ structure resulting in a cubic-to-tetragonal phase transition as cooling the sample through the Curie temperature is not taking place. A plausible reason is that the small size of the $BaTiO_3$ nanocrystals, which are so small that the structural defects in the particles prevent the completion of the structural transition, leading to high strains within the crystals. The high strains inside the nanoparticles introduced by structural defects (e.g., lattice defects) would make the unit cell distortion (c/a ratio) much smaller than that in the standard $BaTiO_3$. To reveal the high strains in the hydrothermal $BaTiO_3$ nanoparticles by TEM images, Zhu et al. [81] recorded both bright- and dark-field TEM images from the hydrothermal $BaTiO_3$ nanoparticles. Figure 4(a) is a bright-field TEM image recorded by using a small objective aperture that selects only the (000) central transmitted beam, which shows narrow-distribution spherical nanoparticles. The dark-field image shown in Figure 4(b) was recorded by using a smaller objective aperture that selects the part of the {100} and {110} reflections, as indicated by a circle in Figure 4(c). The dark-field image displayed in Figure 4(b) clearly shows high strains in some $BaTiO_3$ nanoparticles. By using the bright- and dark-field TEM images, Lu et al. [82] also reported several types of TEM contrast variations in an individual $BaTiO_3$ nanocrystal synthesized *via* hydrothermal method at a temperature of 230°C. It is believed that the different types of variations of TEM contrast indicate the existence of different strains in $BaTiO_3$ nanograins. Therefore, in a TEM image, large strain is indicated by a contrast variation across a particle. If a particle is single crystalline and has no strain, it should be uniform in contrast. However, for a single crystalline particle, if the TEM image shows dark-bright variation in contrast, it is likely to have a high strain within the grain. Strain affects the diffraction behavior of the electrons, resulting in dramatic contrast

http://dx.doi.org/10.5772/61640

change. The hydrothermal $BaTiO_3$ nanoparticles exhibit a cubic structure (a high-temperature phase) at room temperature; such an abnormal crystallographic phenomenon is closely related to the existence of high strains in these $BaTiO_3$ nanoparticles. The strains introduced by a high concentration of lattice defects such as OH^- ions and barium vacancies can make the unit cell distortion (*c*/*a* ratio) much smaller compared with that of the standard $BaTiO_3$. As a result, no peak splitting was detected in the XRD patterns of the hydrothermal $BaTiO_3$ powders even though they belong to the tetragonal phase.

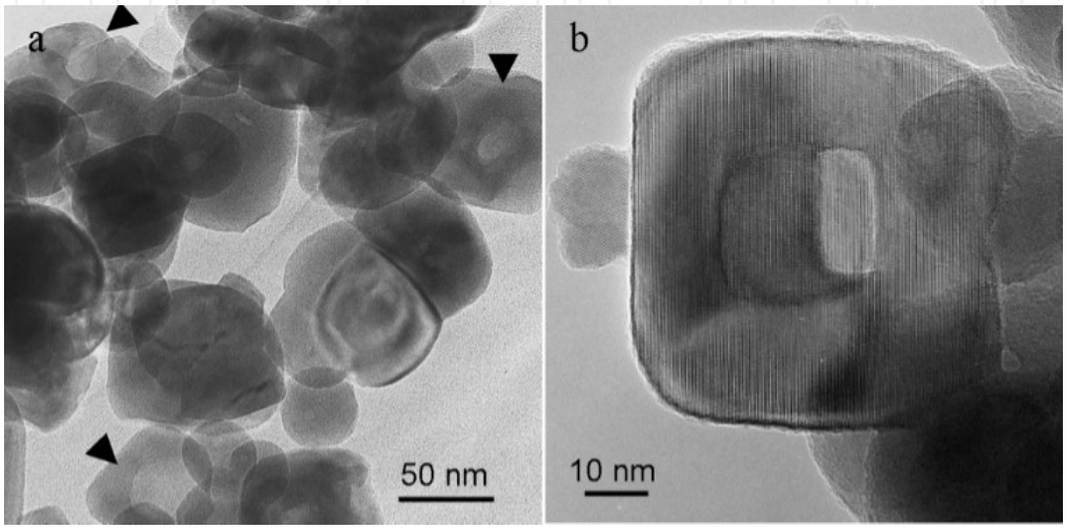

Figure 3. Transmission electron microscopy images of (a) as-received $BaTiO_3$ powder (particle size ~60 nm) and (b) $BaTiO_3$ powder annealed at 673 K. Figures reproduced with permission from [79].

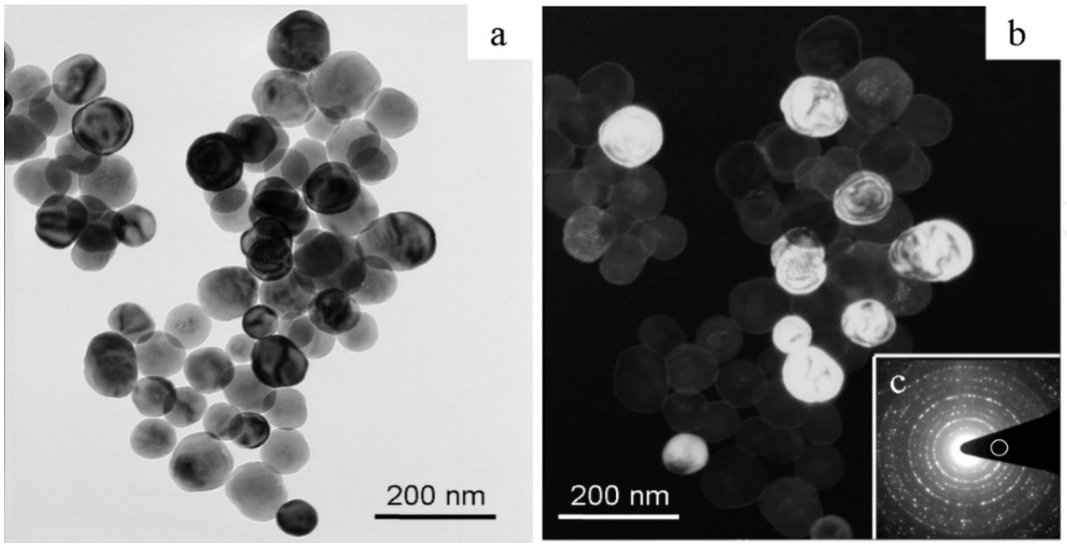

Figure 4. (a) Bright-field and (b) dark-field TEM images recorded from the hydrothermal $BaTiO_3$ nanoparticles. (c) A selected area electron diffraction pattern from the $BaTiO_3$ particles showing a perovskite structure. The circle indicates the size and position of the objective aperture used to record the dark-field image displayed in (b). Figures reproduced with permission from [80].

Due to the ability of revealing the local atomic structures, HRTEM image is the most useful and appropriate technique for identifying the local structures at the edges of perovskite nanocrystals. For example, a terrace-ledge-kink (TLK) surface structure is frequently observed at the edges of the hydrothermal perovskite $BaTiO_3$ [84,85] and $ZnZrO_3$ [86] nanocrystals with rough surface morphology, and in most cases the terraces and ledges lie on the {100} planes, as shown in Figures 5 and 6, respectively. Such a TLK surface structure can be explained by the periodic bond chain theory, which was originally developed by Hartmann and Perdok [87]. The rarely seen {110} surface in the perovskite $BaTiO_3$ and $ZnZrO_3$ nanoparticles were found to be reconstructed so that the surface was composed of corners bound by {100} mini-faces like the triangular small islands.

Internal defect textures, such as nanoscale multiple (111) twining and complicated (111) intergrowth defects, were also observed in the $BaTiO_3$ nanocrystals synthesized by sol–gel and stearic acid-gel (SAG) methods. They were identified as hexagonal-type $BaTiO_3$ structure [88, 89]. Complex arrangements of defects lying on the (111) plane were observed in the SAG-derived $BaTiO_3$ nanocrystal with particle size of 10 nm. The density of the small defects was estimated to be on the order of $10^{27}/m^3$ in the SAG-derived $BaTiO_3$ nanocrystals. These high density of defects could result in the cubic phase structure of SAG-derived $BaTiO_3$ powders even with grain size large up to 3.50 μm [88].

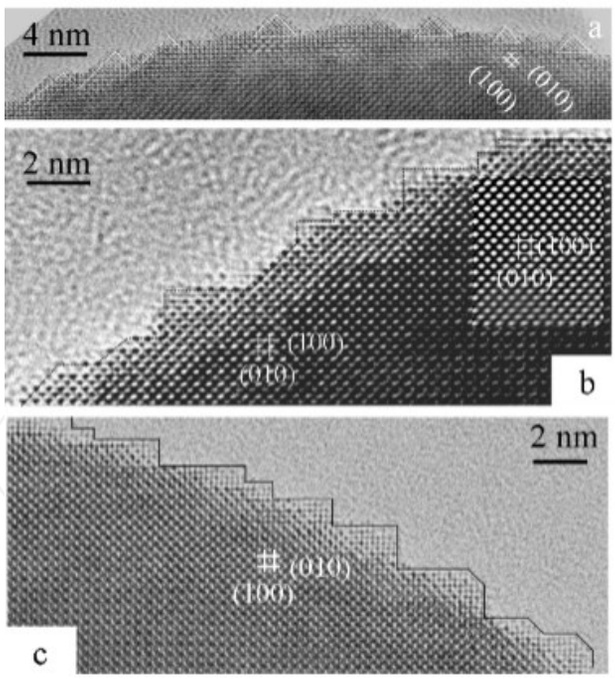

Figure 5. HRTEM images of the surface structures at the edges of $BaTiO_3$ nanoparticles viewed from the [001] direction. (a) Both a terrace-ledge-kink (TLK) surface structure and small nucleated and triangular islands with two to three atomic layer thickness are observed. (b) and (c) TLK surface structure with both terraces and ledges lying on the {100} planes; only a small amount of ledges lie on the (110) plane. The inset in (b) is a Fourier-filtered image of the corresponding position, which clearly demonstrates two perpendicular sets of (100) and (010) planes. Reproduced with permission from [84].

http://dx.doi.org/10.5772/61640

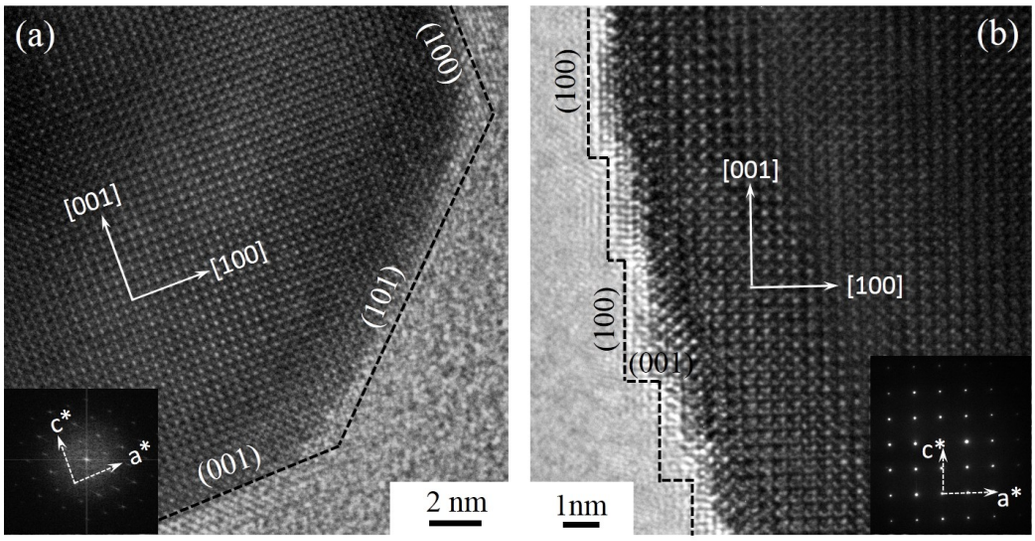

Figure 6. HRTEM images of the surface structures at the edges of perovskite $ZnZrO_3$ nanocrystals synthesized at different Zn/Zr molar ratios in the precursors. (a) Zn/Zr = 3.0, and (b) Zn/Zr = 4.0. Inset in Figure a is the FFT patterns of the corresponding HRTEM image, and inset in Figure d is the SAED pattern taken from the [010]-zone axis. The {100} and (101) facets are indicated in Figure a, and surface steps lying on the {100} planes are indicated in Figure b. Reproduced with permission from [86].

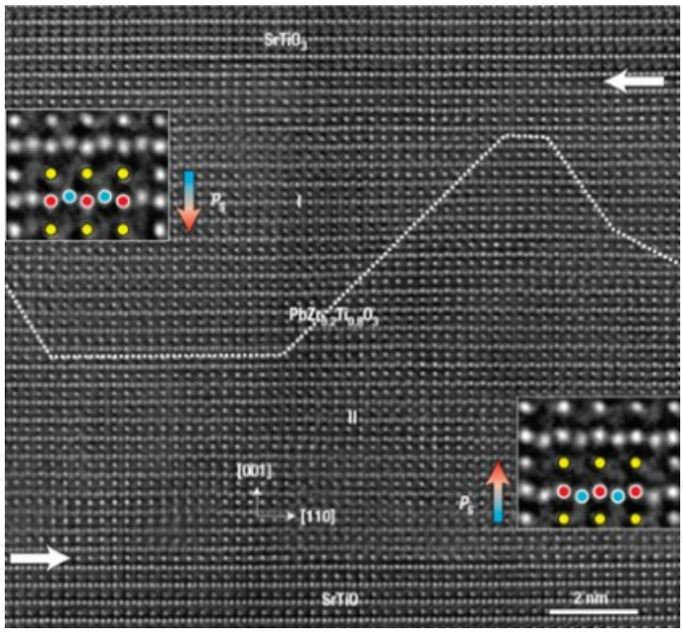

Figure 7. Atomic-scale imaging of the electric dipoles formed by the relative displacements of the Zr/Ti cation columns and the O anion columns in the approximately 10-nm-thick $PbZr_{0.2}Ti_{0.8}O_3$layer sandwiched between two $SrTiO_3$ layers. The image was viewed along the [] direction and recorded under negative spherical-aberration imaging conditions. The atom columns appear bright on a dark background. The horizontal arrows denote the horizontal interfaces between the $PbZr_{0.2}Ti_{0.8}O_3$ film and the top and the bottom $SrTiO_3$ film layers. The dotted line traces the 180° domain wall between the domain I and domain II. The arrows denoted by 'P_S' show the directions of the polarization in the 180° domains. Two insets show higher magnifications of the dipoles formed by the displacements of ions in the unit cells. Yellow symbols denote PbO atom columns seen end-on, red symbols for Zr/Ti columns, and blue symbols for oxygen. Reproduced with permission from [92].

Traditionally, spherical aberration (Cs) of magnetic lenses limits the resolutions of HRTEM and STEM images. In recent years, spherical aberration correctors (e.g., hexapole type Cs-correctors proposed by Rose [90]) have been developed to substantially reduce the effective value of Cs of the objective lens. The Cs-corrected HRTEM mode offers a tunable spherical aberration coefficient from negative to positive values. Properly combining a negative Cs with a positive defocus, at no cost to point resolution, an HRTEM image with bright-contrast of atoms on dark background can be obtained, which can be directly interpreted without image simulation, and light elements such as oxygen atoms and even their vacancies can also be imaged [91,92]. For example, by using the Cs-corrected imaging technique, Jia et al. [92] first performed the atomic-scale investigations of the electric dipoles near (charged and uncharged) 180° domain walls in thin epitaxial $PbZr_{0.2}Ti_{0.8}O_3$ film sandwiched between two $SrTiO_3$ layers. Figure 7 is an atomic-scale image of the electric dipoles formed by the relative displacements of the Zr/Ti cation columns and the O anion columns in $PbZr_{0.2}Ti_{0.8}O_3$ film, viewed from the direction and recorded under negative spherical-aberration imaging conditions. The local tetragonality c/a and spontaneous polarization inside the domains and across the domain wall were calculated. For the first time, a large difference in atomic details between charged and uncharged domain walls was reported. Such breakthrough would improve our ability to see and thoroughly explore the properties of perovskite nanocrystals. We can foresee that the new Cs-corrected HRTEM and STEM will benefit perovskite nanopowder materials research in the new era.

4. Properties of perovskite nanocrystals

4.1. Ferroelectric and dielectric properties

Perovskite $BaTiO_3$ nanocrystals can be used as initial building blocks to fabricate thin films, which exhibit highly uniform nanostructured texture and grain sizes. Recently, well-isolated $BaTiO_3$ nanocrystals smaller than 10 nm with control over aggregation and crystal densities have been synthesized and used to construct films with a uniform nanocrystalline grain texture [93]. The ferroelectric behavior was found in these $BaTiO_3$ nanocrystallined films with grain sizes in the range of 10–30 nm. Their relative dielectric constants were in the range of 85–90 over the 1–100 KHz with low dielectric loss of 0.03–0.04, representing a promising application in thin-film capacitance [93]. The nanometer-scale ferroelectric property of tetragonal $BaTiO_3$ particles with sizes of 6–12 nm is also reported by Nuraje et al. [94]. The ferroelectric polarization of these nanoparticles can be manipulated by electrostatic force microscopy (EFM), as demonstrated in Figure 8. First, the electric polarization of the $BaTiO_3$ nanoparticles was manipulated by applying a voltage, V_{write}, to the conductive atomic force microscopy(AFM) tip that gently contacts the nanoparticles (Figure 8a). After the local electric polarization is written onto the nanoparticles, the resulting polarization is probed using EFM with a lower voltage, V_{probe}, by measuring the shift in the resonance frequency of the AFM tip. As shown in Figure 8(a), during the probing process the AFM tip is raised at a constant height above the nanoparticles in order to avoid interference between the manipulated polarization and V_{probe}. The raised distance of 50 nm enables one to image only the contribution from the surface charges associated with the local electric polarization of the $BaTiO_3$ nanoparticles. After a V_{write} of +12 V was applied to $BaTiO_3$ nanoparticles with an average diameter of 12 nm (Figure 8b),

http://dx.doi.org/10.5772/61640

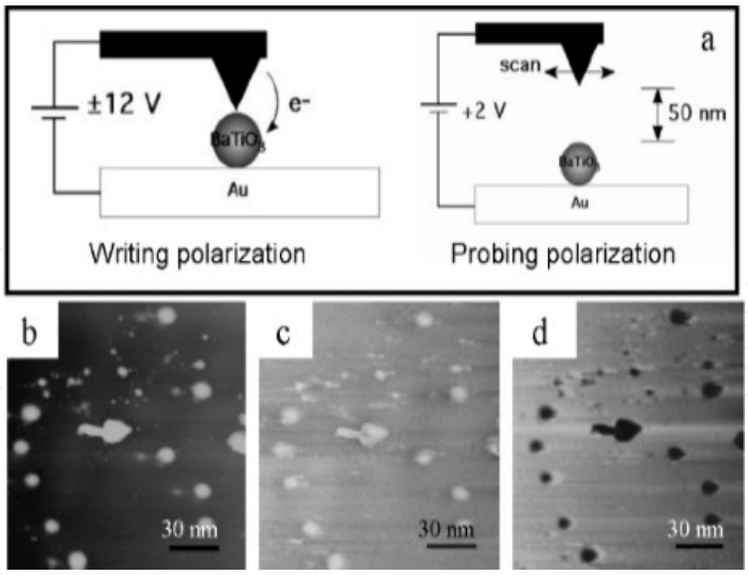

Figure 8. (a) Schematic diagram of manipulating and probing the electric polarization of $BaTiO_3$ nanoparticles with EFM. (b) Topological AFM image of $BaTiO_3$ nanoparticles. (c) and (d) EFM images of $BaTiO_3$ nanoparticles with V_{probe} = +2 V after V_{write} = ± 12 V was applied on the nanoparticles across a conductive AFM tip and a gold substrate. Reproduced with permission from [95].

the EFM image of those nanoparticles to which a V_{probe} of +2 V was applied, shown in Figure 8(c), appears in a brighter contrast compared with the background due to the repulsive electrostatic interaction between the tip and the nanoparticles. After a V_{write} of –12 V applied to the same $BaTiO_3$ nanoparticles, the EFM image of those nanoparticles to which a V_{probe} of –2 V was applied, shown in Figure 8(d), appears in a darker contrast compared with the background due to the attractive electrostatic interaction. It should be noted that the experiments that involved scanning the manipulated nanoparticles with V_{probe} = –2 V resulted in reverse EFM images, which confirms that the probe voltage did not interfere significantly with the written polarization. These EFM images indicate that the $BaTiO_3$ nanoparticles synthesized in the peptide nanorings at room temperature possess a ferroelectric property with spontaneous electric polarization, which can be reoriented by an external electric field.

4.2. Magnetic properties

The magnetic properties of perovskite oxide nanocrystals are dependent upon the particle size or large surface-area-to-volume ratio. For most biomedical and magnetofluidic applications, magnetic nanoparticles with fairly uniform size and having a Curie temperature above room temperature are highly required. In this application, a well-controlled, reproducible, and narrow distribution of ferromagnetic nanoparticle sizes is important in addition to having a large magnetic moment per particle. Lipham et al. [99] have synthesized polycrystalline, nanometer-sized powders of $La_{1-x}SrxMnO_3$ by a citrate gel technique. The particle sizes of which were in the range of 11–17 nm, their saturated magnetizations at 300 K in the range of 7–26 emu/g, and magnetic transition temperature from 275 to 350K. The saturated magnetization and magnetic transition temperature increased linearly with increasing the average particle size.

The magnetic properties of single-crystalline multiferroic $BiFeO_3$ nanoparticles were also reported by Park et al. [100] and Selbach et al. [101]. Their results demonstrate that the $BiFeO_3$ nanoparticles exhibit strong size-dependent magnetic properties that correlate with: (a) increased suppression of the known spiral spin structure (period length of ~62 nm) with decreasing nanoparticle size and (b) uncompensated spins and strain anisotropies at the surface. Both zero-field-cooled and field-cooled magnetization curves exhibit spin-glass freezing behavior due to a complex interplay between finite size effects, inter-particle interactions, and a random distribution of anisotropy axes in the nanoparticle assemblies.

4.3. Multiferroic properties

Multiferroic materials are characterized by the coexistence of spin, orbital, and/or electric-dipole orders and cross-term effects between the corresponding different degrees of freedom [102,103]. Magnetoelectric (ME) multiferroics are an example of materials that combine simultaneously ferromagnetic and ferroelectric in the same phase, with coupling between the two orders. That implies they possess spontaneous magnetization which can be reoriented by an applied magnetic field, and spontaneous polarization which can be reoriented by an applied electric field. Up to date, large ME effects have been observed in the form of ferroelectric phase transitions induced by magnetic fields in perovskite manganites [104] and switching local ferromagnetism by an electric field through the coupling between multiferroic $BiFeO_3$ and a ferromagnet [105,106]. Magnetoelectric memory effects and magnetic switching of ferroelectric domains (and the converse process) have been demonstrated in many multiferroic materials. By using an optical second harmonic generation technique ferrotoroidic domains are spatially revealed in $LiCoPO_4$ multiferroics, where independent antiferromagnetic domains exist; with this method, the coupling between magnetic and electric domains is also confirmed [107]. Due to the weak coupling behaviors between the ferroelectric and the magnetic order parameters in the single-phase multiferroics and small values of the electric and magnetic polarizations at room temperature, the applications of single-phase multiferroics are not very attractive in the near future. However, for the single-phase multiferroics, there still exist some basic questions to be answered such as the origin of the ferroelectricity in some unusual multiferroics [104]. Up to date, several coupling mechanisms between the magnetic and ferroelectric ordering in the single-phase multiferroics have been proposed and extensively investigated; it is still unclear how to obtain high-temperature single-phased ferromagnetic–ferroelectric multiferroicity. From a viewpoint of the practical applications, it is very important and is still a major challenge to develop robust room-temperature ferromagnetic ferroelectrics that are sufficiently insulating to sustain a large macroscopic polarization [108].

5. Applications of perovskite oxide nanocrystals

Due to their high dielectric, ferroelectric, piezoelectric, pyroelectric, and electro-optic properties, perovskite oxide nanocrystals have wide ranges of applications, such as multilayered ceramic capacitors, ferroelectric memories, voltage tunable capacitors, surface acoustic wave devices, microactuators, and IR detectors. An emerging application seeks to exploit the

http://dx.doi.org/10.5772/61640

multiferroic properties of perovskite oxide nanocrystals to develop novel multifunctional devices controlled by magnetic and electric fields. This magnetoelectric coupling enables the manipulation of the ferroelectric polarization by a magnetic field [104] or the control of the antiferromagnetic vector orientation by an electric field [105]. This latter opportunity is very appealing for spintronics as it may allow to control the magnetization of a ferromagnet, exchange coupled to a ferroelectric antiferromagnet, through an electric field. In other words, it may enable electrical writing of magnetic information with a low power consumption, like an magnetic random access memory(MRAM) cell [109]. In the subsequent sections, typical applications of perovskite oxide nanocrystals are introduced.

5.1. Nanoelectronics

An important application of perovskite oxide nanocrystals in electronics is the multilayered ceramic capacitors(MLCCs). The MLCCs based on $BaTiO_3$ powders have used in many electronic devices such as video camera, cell phone, laptop computers, and automobiles. Two key features of the MLCCs have attracted high degree of interest in them. One is the discovery of the ferroelectric properties of perovskite $BaTiO_3$ and its high relative dielectric constant. The other is the technical breakthrough for making multilayer ceramic units in a small volume, thus satisfying the need for an economical manufacture of systems, and the requirements for printed circuit boards and for hybrid circuits on ceramic substrates. With increasing the volumetric efficiency of electronic devices, MLCCs are needed to use much thin dielectric layers. Recently, it is expected that the dielectric layers as thin as 1 μm or less will be available in MLCCs for the next generation of electronic components. Besides the thin dielectric layers, other key factors for the development of future highly volume-efficient and high-capacitance MLCCs should be considered, such as the use of high dielectric films, large numbers of active dielectric layers, improvement in the overlap area, and stacking precision of the electrodes. For ideal $BaTiO_3$ nanopowders used for the next generation MLCCs, they should have high purity, homogeneous compositions and cation distributions, uniform sizes and shapes, and weak agglomeration. Generally, solution-based techniques are used to prepare such very fine powders, since these techniques could synthesize homogeneous, phase-pure, and stoichiometric $BaTiO_3$ nanocrystals with finer particle sizes due to the finer scale of mixing and subsequently lower processing temperature.

5.2. Information storage devices

Ferroelectric materials possess an electric dipole moment even in the absence of an external electric field. Such a spontaneous polarization is caused by the positional bistability of constituent ions in the crystal and its direction can be adjusted by an external field. Since the response time of the ion displacement is the order of ns or less, so non-volatile random access memory called FeRAM (ferroelectric random access memory) can be realized using ferroelectric capacitors, in which two states of “0” and “1” in the binary logic are represented by the direction of the spontaneous polarization. Two different types of FeRAM cells can be used to achieve data storage and read operations, which are named as 1T-1C and 2T-2C configurations [110]. Because the 2T-2C cell occupies a large area, it is only used for FeRAM memories with

densities of 256 kbit or less. A significantly smaller cell size can be achieved by eliminating the complementary reference capacitor in each cell and accessing a reference signal from a single reference capacitor placed outside the cell array. The cell size in 1T-1C configuration is reduced because only one transistor and one capacitor are required to form the popular cell. In the FeRAM cell, the polarization direction is set by a positive or negative voltage pulse to the ferroelectric capacitor defining logical "0" or "1". For readout, another voltage pulse is applied and the stored bit configuration determines whether or not the polarization switched direction. The ferroelectric capacitor suffers from the fact that data are destroyed during readout and bit reprogramming is required after each read cycle, i.e., the data read process is destructive. As a result, switching the polarization during both write and read operations would cause reduced endurance, resulting in short lifetime of FeRAM cells because of the fatigue problem of the ferroelectric material. In addition, during the read-processing data storage is volatile and data could be erased if powder supply is lost during the reading process. To overcome the destructive readout scheme of FeRAM, recently considerable efforts have focused on the development of a so-called ferroelectric gate field-effect transistor (FeFET). The principle of a ferroelectric-gate field-effect transistor is based on a conventional Si MOSFET (metal oxide semiconductor ferroelectric-gate field effect transistor) whose gate dielectrics is a ferroelectric materials. This FET-type FeRAMs have such unique features as non-volatile data storage, non-destructive data readout, and the single-transistor-type cell structure. Further advantages are the reduced power consumption and better scaling properties as in the case of usual FeRAM cells. Although the FET-type FeRAMs have been studied since the 1950s [111], however, up to date the commercially available devices have not been fabricated, mainly due to the interfacial structures between the perovskite ferroelectric and a semiconductor. Any imperfections at the interface, such as the formation of undesirable phases or electronic trapping states, will seriously degrade the performance of the device. Essential challenges for the FeFET are the improvement of the retention time and the suppression of serious parasitic effects such as the charge traps at the Si–ferroelectric interface. One possible solution in the case of a FeFET is the incorporation of one insulating buffer layer between the Si and the ferroelectric, which is composed of either a dielectric material (MFIS structure) or a stacked structure of conductive and dielectric materials (MFMIS structure). Several buffer layers such as SiO_2, CeOx, and Si_3N_4 have been investigated. The most recent results by using alternative gate oxides such as HfO_2 or HfAlO show encouraging results, and the retention time for the gate layer sequence of Pt/SBT/HfO_2/Si is up to 30 days [112]. However, insertion of the buffer layer causes new problems such as current injection that lead to short data retention time. Another considered factor is the leakage current of both the ferroelectric film and the buffer layer. If the charge neutrality at a node between the two capacitors is destroyed by the leakage current, electric charges on the electrodes of the buffer layer capacitor disappear, which means that carriers on the semiconductor surface disappear and the stored data cannot be readout by drain current of the FET, even if the polarization of the ferroelectric film is retained. FeFET based on epitaxial perovskite heterostructures was also demonstrated, in which doped rare-earth manganates such as $La_{0.7}Ca_{0.3}MnO_3$ were used as the semiconductor channel material, and $Pb(Zr_{0.2}Ti_{0.8})O_3$ as the ferroelectric gate in the prototypical epitaxial field effect device [112]. The carrier concentration of the semiconductor channel can be tuned by varying the manganate stoichi-

http://dx.doi.org/10.5772/61640

ometry. The enhanced interface characteristics associated with the ferroelectric-manganate interface allows for the fabrication of field effect devices with channel resistance modulation of at least a factor of 3 and retention on the order of hours.

Perovskite oxide nanocrystals also exhibit good dielectric properties, which can be used for dynamic random access memory (DRAM). The DRAM is the primary working medium for information storage in the microelectronic devices that comprise the entire litany of electronic systems. DRAM works by using a submicron-sized capacitor, representing one bit of memory, to store a given amount of electrical charge: if the charge is present, it represents a digital "1", if not then the bit is a "0". Each bit is addressed using a complementary metal oxide semiconductor field effect transistor, which acts as a valve for adding to or removing charge from the capacitor upon application of a voltage. Conventional DRAMs employ either SiO_2 capacitors, or a combination of SiO_2 and Si_3N_4 nitride, which is termed ONO (oxy-nitride). The next generation of DRAMs will utilize Ta_2O_5 replacing ONO, but the tantalum oxide relative dielectric constant is only about 25, and it appears that the DRAM evolution will skip this intermediate stage and pass directly to very high dielectric materials ($\varepsilon_r = 500 – 1500$) that are ferroelectric or nearly ferroelectric. Many of these materials are perovskite oxides with ABO_3 perovskite, or closely related variations of perovskites. Several good reviews of this technology are given by Gnade et al. [113], Tasch and Parker [114], and Scott [115]. In going from 64 Mbit to 4 Gbit DRAM, the most promising dielectric material is perovskite barium strontium titanate (BST), which can be processed by physical deposition, especially sputtering with good results [116]. A dielectric material should have a low leakage current and high dielectric constant, and it is desirable to use the paraelectric BST for DRAM. Among the $Pb(Zr,Ti)O_3$ (PZT), $SrTiO_3$, and BST ferroelectric materials, $(Ba,Sr)TiO_3$ is the most promising material for DRAM capacitors because it is a better insulator with a higher dielectric constant than PZT and $SrTiO_3$, and it can be controlled to be the paraelectric phase with an appropriate ratio of Ba/Sr composition [117].

5.3. Spintronics

Applications of the magnetoelectric coupling and multiferroics in the fields of spintronics are increasing rapidly, and numerous possible device architectures have been proposed and fabricated [118]. For example, in the ferroelectric antiferromagnets, such as the multiferroic perovskites, the magnetic structure could be modulated or controlled by the application of an electric field [119,120]. For example, non-volatile control of the orientation of the antiferromagnetic axis can be achieved by using the coupling between ferroelectricity and antiferromagnetism that can provide permanent [121]. Similarly, the coupling between the antiferromagnetic component and an adjacent ferromagnet also allows to switch the ferromagnetism by the application of an electric field. Therefore, potential new types of multiple-state memories and spintronic devices controlled by electric and magnetic fields can be developed. One specific demonstration is a multiferroic tunnel junction used as a spin filter device with the potential to control both electrically and magnetically [122,123]. In such a spin filter device, the multiferroic tunnel barrier should be as thin as 1–2 nm thickness. Experiments and theoretical calculations show that a critical thickness of a few unit cells is closely related to the screening properties of the electrodes [124,125]. Another potential application of multiferroics in spintronics is the spin wave devices controlled by electric field. Smolenskii

and Chupis theoretically analyzed the excitation of spin waves by an alternating electric field, and of ferroelectric oscillations by a magnetic field [126], and concluded that such excitations should be strongest in ferroelectric ferrimagnets, which could be used to produce magneto-electric generators or spin wave amplifiers driven by electric field or current. Up to now, few works on the influence of electric fields on spin waves are reported. Recently, Pimenov et al. first demonstrated such hybrid excitations in multiferroic manganites 125]. It is expected that this field should be a hot topic in near future.

6. Future outlook of perovskite nanocrystals

Perovskite nanopowdes (e.g., $BaTiO_3$) are widely used in MLCCs in the electronic industry due to their excellent dielectric properties. In recent years, miniaturization of ferroelectric $BaTiO_3$ powders to the nanometer scale is very desirable for their applications in the next generation of electronics; however, the main challenge lies in the synthesis of barium titanate nanocrystals at room temperature with a tetragonal crystalline structure, which induces the ferroelectric property. Much effort has been concentrated on synthesizing the high-purity, homogeneous, weakly agglomerated nanocrystals with tetragonal structure. However, it is known that the ferroelectricity becomes weaker with a decrease in particle size and disappears below a certain critical size, known as the size effect. Lots of fundamental and experimental studies are needed to understand the size effect of ferroelectricty for nanosized perovskite powders, to develop future high volume-efficient and high-capacitance MLCCs.

Perovskite oxide nanocrystals also exhibit multiferroic behavior, which is the fundamental of giant ME effects and ME phase control. However, these phenomena are now primarily investigated in the viewpoint of basic research rather than the practical applications. The main reason is that the number of multiferroic compounds with perovskite structure is very small, in many cases use of bulk single crystals is necessary and only very few multiferroics exhibit ME behavior at room temperature. Several microscopic physical mechanisms of ME behaviours in multiferroics have been revealed and the precise criteria searching for new multiferroics have been given out. More and more perovskite multiferroics will be developed and the improvement on tuning the ME performance will drive multiferroics much closer to practical applications in the near future. Now, the major challenge is developing the room-temperature perovskite multiferroics insulators and expanding their applications in the fields of micro-electronics.

7. Conclusions

In this chapter, we have reviewed various processing routes, characterization, functionalization, and novel application areas of perovskite oxide nanocrystals. Significant progress has been achieved in the development of processing routes for perovskite oxide nanocrystals, which ranges from the solid-state reaction to chemical solution depositions. By introducing

the $BaTiO_3$ nanoparticles into the multilayer dielectrics, much advancement has been achieved in reducing dielectric thickness and increasing the volumetric efficiency of $BaTiO_3$-based MLCCs, to meet the miniaturization demand for electronic devices. At the nanoscale, highly accurate microstructural characterizations are usually required for investigating the microstructures of perovskite nanocrystals. The unique properties of perovskite oxide nanocrystals (e.g., ferroelectric and dielectric, electrical, magnetic, and multiferroic properties) are addressed based on the selected recent literature. An important conclusion from the extensive review is that there exists size effects for these unique properties. Better understanding of the size effects in perovskite oxide nanocrystals will be helpful in selecting the critical size and dimension for the purpose of implementing perovskite oxide nanocrystals in various devices. Applications of perovskite oxide nanocrystals have been identified with a major focus in areas such as nanoelectronics, information storage devices, and their potential applications in spintronics are also briefly introduced. As research into perovskite oxide nanocrystals spreads its wings, becoming more extensive, a complete review on this subject has become an arduous task. However, in this chapter a modest attempt is made to analyze recent significant developments in researches of perovskite oxide nanocrystals and their possible applications in various industries.

Acknowledgements

This work is partially supported by National Natural Science Foundation of China (grant nos. 11174122 and 11134004), National Basic Research Program of China (grant no. 2015CB654900), the open project from National Laboratory of Solid State Microstructures, Nanjing University (grant no. M26012), and six big talent peak project from Jiangsu province (grant no. XCL-004).

Author details

Heng Wu and Xinhua Zhu*

*Address all correspondence to: xhzhu@nju.edu.cn

National Laboratory of Solid State of Microstructures, School of Physics, Nanjing University, Nanjing, China

References

[1] Schaak RE, Mallouk TE. Perovskites by design: a toolbox of solid-state reactions. Chem Mater 2002;14(4):1455–71. DOI: 10.1021/cm010689m

[2] Bhalla A, Guo R, Roy R. The perovskite structure–a review of its role in ceramic science and technology. Mater Res Innovat 2000;4(1):3–26. DOI: 10.1007/s100190000062

[3] Dawber M, Rabe K, Scott J. Physics of thin-film ferroelectric oxides. Rev Mod Phys 2005;77(4):1083–130. DOI: 10.1103/RevModPhys.77.1083

[4] Gruverman A, Kholkin A. Nanoscale ferroelectrics: processing, characterization and future trends. Rep Prog Phys 2006;69(8):2443–74. DOI: 10.1088/0034-4885/69/8/R04

[5] Hill NA. Why are there so few magnetic ferroelectrics. J Phys Chem B 2000;104(29): 6694–709. DOI: 10.1021/jp000114x

[6] Fiebig M, Lottermoser T, Frohlich D, Goltsev AV, Pisarev RV. Observation of coupled magnetic and electric domains. Nature 2002;419(6909):818–20. DOI: 10.1038/nature01077

[7] Wang J, Neaton JB, Zheng H, Nagarajan V, Ogale SB, Liu B, et al. Epitaxial $BiFeO_3$ multiferroic thin film heterostructures. Science 2003;299(5613):1719–22. DOI: 10.1126/science.1080615

[8] Hur N, Park S, Sharma PA, Ahn JS, Guha S, Cheong SW. Electric polarization reversal and memory in a multiferroic material induced by magnetic fields. Nature 2004;429(2990):392–5. DOI: 10.1038/nature02572

[9] Haertling GH. Ferroelectric ceramics: history and technology. J Am Ceramic Soc 1999;82(4):797–818. DOI: 10.1111/j.1151-2916.1999.tb01840.x

[10] Moulson AJ, Herbert JM. Electroceramics: Materials, Properties, Applications. 1st ed. New Jersey, USA: John Wiley & Sons; 2003. 557 p. DOI: 10.1002/0470867965

[11] Yoon DH, Lee BI. $BaTiO_3$ properties and powder characteristics for ceramic capacitors. J Ceramic Process Res 2002;3(2):41–7.

[12] Yoon D. Tetragonality of barium titanate powder for a ceramic capacitor application. J Ceramic Process Res 2006;7(4):343.

[13] Pithan C, Hennings D, Waser R. Progress in the synthesis of nanocrystalline $BaTiO_3$ powders for MLCC. Int J Appl Ceramic Technol 2005;2(1):1–14. DOI: 10.1111/j.1744-7402.2005.02008.x

[14] Chu MS, Rae AW. Manufacturing dielectric powders. Am Ceramic Soc Bull 1995;74(6):69–72.

[15] Hu YH, Harmer MP, Smyth DM. Solubility of BaO in $BaTiO_3$. J Am Ceramic Soc 1985;68(7):372–6. DOI: 10.1111/j.1151-2916.1985.tb10145.x

[16] Phule P, Risbud S. Low-temperature synthesis and processing of electronic materials in the BaO-TiO_2 system. J Mater Sci 1990;25(2):1169–83. DOI: 10.1007/BF00585422

[17] Joshi UA, Lee JS. Template-free hydrothermal synthesis of single-crystalline barium titanate and strontium titanate nanowires. Small 2005;1(12):1172–6. DOI: 10.1002/smll.200500055

[18] Niederberger M, Pinna N, Polleux J, Antonietti M. A general soft-chemistry route to perovskites and related materials: synthesis of $BaTiO_3$, $BaZrO_3$, and $LiNbO_3$ nanoparticles. Angewandte Chemie International Edition 2004;43(17):2270–3. DOI: 10.1002/anie.200353300

[19] Templeton LK, Pask JA. Formation of $BaTiO_3$ from $BaCO_3$ and TiO_2 in air and in CO_2. J Am Ceramic Soc 1959;42(5):212–6. DOI: 10.1111/j.1151-2916.1959.tb15455.x

[20] Buscaglia MT, Bassoli M, Buscaglia V, Alessio R. Solid-state synthesis of ultrafine $BaTiO_3$ powders from nanocrystalline $BaCO_3$ and TiO_2. J Am Ceramic Soc 2005;88(9):2374–9. DOI: 10.1111/j.1551-2916.2005.00451.x

[21] Beauger A, Mutin JC, Niepce JC. Synthesis reaction of metatitanate $BaTiO_3$. J Mater Sci 1983;18(10):3041–6. DOI: 10.1007/BF00700786

[22] Ubaldini A, Buscaglia V, Uliana C, Costa G, Ferretti M. Kinetics and mechanism of formation of barium zirconate from barium carbonate and zirconia powders. J Am Ceramic Soc 2003;86(1):19–25. DOI: 10.1111/j.1151-2916.2003.tb03271.x

[23] Kimura T. Molten salt synthesis of ceramic powders. In: Sikalidis C. (Ed.) Advances in Ceramics-Synthesis and Characterization, Processing and Specific Applications. 1st ed. Rijeka, Croatia: INTECH Open Access Publisher; 2011. pp. 75–100. DOI: 10.5772/20472

[24] Yang J, Li RS, Li XC, Long YL, Zhou JY, Zhang YM. Molten salt synthesis of $SrFeO_3$ nanocrystals. J Ceramic Soc Jpn 2011;119(1394):736–9. DOI: 10.2109/jcersj2.119.736

[25] Li H-L, Du Z-N, Wang G-L, Zhang Y-C. Low temperature molten salt synthesis of $SrTiO_3$ submicron crystallites and nanocrystals in the eutectic NaCl–KCl. Mater Lett 2010;64(3):431–4. DOI: 10.1016/j.matlet.2009.11.040

[26] Zhou H, Mao Y, Wong SS. Probing structure−parameter correlations in the molten salt synthesis of $BaZrO_3$ perovskite submicrometer-sized particles. Chem Mater 2007;19(22):5238–49. DOI: 10.1021/cm071456j

[27] Shivakumara C. Low temperature synthesis and characterization of rare earth orthoferrites $LnFeO_3$ (Ln=La, Pr and Nd) from molten NaOH flux. Solid State Commun 2006;139(4):165–9. DOI: 10.1016/j.ssc.2006.05.030

[28] Fossdal A, Einarsrud M-A, Grande T. Phase equilibria in the pseudo-binary system $SrO–Fe_2O_3$. J Solid State Chem 2004;177(8):2933–42. DOI: 10.1016/j.jssc.2004.05.007

[29] Yoon K, Cho Y, Kang D. Molten salt synthesis of lead-based relaxors. J Mater Sci 1998;33(12):2977–84. DOI: 10.1023/A:1004310931643

[30] Thirumal M, Jain P, Ganguli AK. Molten salt synthesis of complex perovskite-related dielectric oxides. Mater Chem Phys 2001;70(1):7–11. DOI: 10.1016/S0254-0584(00)00384-9

[31] Chen J, Xing X, Watson A, Wang W, Yu R, Deng J, et al. Rapid synthesis of multiferroic $BiFeO_3$ single-crystalline nanostructures. Chem Mater 2007;19(15):3598–600. DOI: 10.1021/cm070790c

[32] Chen J, Yu R, Li L, Sun C, Zhang T, Chen H, et al. Structure and shape evolution of $Bi_{1-x}La_xFeO_3$ perovskite microcrystals by molten salt synthesis. Eur J Inorg Chem 2008;2008(23):3655–60. DOI: 10.1002/ejic.200800263

[33] He X, Gao L. Synthesis of pure phase $BiFeO_3$ powders in molten alkali metal nitrates. Ceramics Int 2009;35(3):975–8. DOI: 10.1016/j.ceramint.2008.04.013

[34] Zheng XH, Chen PJ, Ma N, Ma ZH, Tang DP. Synthesis and dielectric properties of $BiFeO_3$ derived from molten salt method. J Mater Sci: Mater Electronics 2012;23(5):990–4. DOI: 10.1007/s10854-011-0533-4

[35] Zhu X, Zhou J, Jiang M, Xie J, Liang S, Li S, et al. Molten salt synthesis of bismuth ferrite nano- and microcrystals and their structural characterization. J Am Ceramic Soc 2014;97(7):2223–32. DOI: 10.1111/jace.12897

[36] Frey MH, Payne DA. Synthesis and processing of barium titanate ceramics from alkoxide solutions and monolithic gels. Chem Mater 1995;7(1):123–9. DOI: 10.1021/cm00049a019

[37] Hwang U-Y, Park H-S, Koo K-K. Low-temperature synthesis of fully crystallized spherical $BaTiO_3$ particles by the gel–sol method. J Am Ceramic Soc 2004;87(12):2168–74. DOI: 10.1111/j.1151-2916.2004.tb07486.x

[38] Brutchey RL, Morse DE. Template-free, low-temperature synthesis of crystalline. Angewandte Chemie 2006;118(39):6714–6. DOI: 10.1002/ange.200602571

[39] Kiss K, Magder J, Vukasovich MS, Lockhart RJ. Ferroelectrics of ultrafine particle size: I, synthesis of titanate powders of ultrafine particle size. J Am Ceramic Soc 1966;49(6):291–5. DOI: 10.1111/j.1151-2916.1966.tb13265.x

[40] Yoon S, Baik S, Kim MG, Shin N. Formation mechanisms of tetragonal barium titanate nanoparticles in alkoxide–hydroxide sol-precipitation synthesis. J Am Ceramic Soc 2006;89(6):1816–21. DOI: 10.1111/j.1551-2916.2006.01056.x

[41] Yoon S, Baik S, Kim MG, Shin N, Kim I. Synthesis of tetragonal barium titanate nanoparticles via alkoxide–hydroxide sol-precipitation: effect of water addition. J Am Ceramic Soc 2007;90(1):311–4. DOI: 10.1111/j.1551-2916.2006.01361.x

[42] Dutta PK, Gregg JR. Hydrothermal synthesis of tetragonal barium titanate ($BaTiO_3$). Chem Mater 1992;4(4):843–6. DOI: 10.1021/cm00022a019

[43] Clark I, Takeuchi T, Ohtori N,C, Sinclair D. Hydrothermal synthesis and characterisation of $BaTiO_3$ fine powders: precursors, polymorphism and properties. J Mater Chem 1999;9(1):83–91. DOI: 10.1039/A805756G

[44] Lee HS, Lee JJ, Chang TS, Kim JW, Koo SM. Hydrothermal synthesis for large barium titanate powders at a low temperature: effect of titania aging in an alkaline solution. J Am Ceramic Soc 2007;90(9):2995–7. DOI: 10.1111/j.1551-2916.2007.01828.x

[45] Choi GJ, Kim HS, Cho YS. $BaTiO_3$ particles prepared by microwave-assisted hydrothermal reaction using titanium acylate precursors. Mater Lett 1999;41(3):122–7. DOI: 10.1016/S0167-577X(99)00117-2

[46] Newalkar BL, Komarneni S, Katsuki H. Microwave-hydrothermal synthesis and characterization of barium titanate powders. Mater Res Bull 2001;36(13–14):2347–55. DOI: 10.1016/S0025-5408(01)00729-2

[47] Khollam YB, Deshpande AS, Patil AJ, Potdar HS, Deshpande SB, Date SK. Microwave-hydrothermal synthesis of equi-axed and submicron-sized $BaTiO_3$ powders. Mater Chem Phys 2001;71(3):304–8. DOI: 10.1016/S0254-0584(01)00286-3

[48] Chen D, Jiao X. Solvothermal synthesis and characterization of barium titanate powders. J Am Ceramic Soc 2000;83(10):2637–9. DOI: 10.1111/j.1151-2916.2000.tb01606.x

[49] Kwon S-G, Choi K, Kim B-I. Solvothermal synthesis of nano-sized tetragonal barium titanate powders. Mater Lett 2006;60(7):979–82. DOI: 10.1016/j.matlet.2005.10.089

[50] Kolen'ko YV, Kovnir KA, Neira IS, Taniguchi T, Ishigaki T, Watanabe T, et al. A novel, controlled, and high-yield solvothermal drying route to nanosized barium titanate powders. J Phys Chem C 2007;111(20):7306–18. DOI: 10.1021/jp0678103

[51] Viviani M, Lemaitre J, Buscaglia MT, Nanni P. Low-temperature aqueous synthesis (LTAS) of $BaTiO_3$: a statistical design of experiment approach. J Eur Ceramic Soc 2000;20(3):315–20. DOI: 10.1016/S0955-2219(99)00150-8

[52] Ciftci E, Rahaman MN, Shumsky M. Hydrothermal precipitation and characterization of nanocrystalline $BaTiO_3$ particles. J Mater Sci 2001;36(20):4875–82. DOI: 10.1023/A:1011828018247

[53] Thomas R, Varadan VK, Komarneni S, Dube DC. Diffuse phase transitions, electrical conduction, and low temperature dielectric properties of sol–gel derived ferroelectric barium titanate thin films. J Appl Phys 2001;90(3):1480–8. DOI: 10.1063/1.1367318

[54] Zhang HX, Kam CH, Zhou Y, Han XQ, Buddhudu S, Xiang Q, et al. Green upconversion luminescence in Er^{3+}:$BaTiO_3$ films. Appl Phys Lett 2000;77(5):609–11. DOI: 10.1063/1.127060

[55] Cho W-S. Structural evolution and characterization of BaTiO3 nanoparticles synthesized from polymeric precursor. J Phys Chem Solids 1988;59(5):659–66. DOI: 10.1016/S0022-3697(97)00227-8

[56] Liu C, Zou B, Rondinone AJ, Zhang ZJ. Sol−gel synthesis of free-standing ferroelectric lead zirconate titanate nanoparticles. J Am Chem Soc 2001;123(18):4344–5. DOI: 10.1021/ja001893y

[57] Pinceloup P, Courtois C, Vicens J, Leriche A, Thierry B. Evidence of a dissolution–precipitation mechanism in hydrothermal synthesis of barium titanate powders. J Eur Ceramic Soc 1999;19(6–7):973–7. DOI: 10.1016/S0955-2219(98)00356-2

[58] Hertl W. Kinetics of barium titanate synthesis. J Am Ceramic Soc 1988;71(10):879–83. DOI: 10.1111/j.1151-2916.1988.tb07540.x

[59] Hu MZC, Kurian V, Payzant EA, Rawn CJ, Hunt RD. Wet-chemical synthesis of monodispersed barium titanate particles -hydrothermal conversion of TiO_2 microspheres to nanocrystalline $BaTiO_3$. Powder Technol 2000;110(1–2):2–14. DOI: 10.1016/S0032-5910(99)00262-4

[60] Eckert JO, Hung-Houston CC, Gersten BL, Lencka MM, Riman RE. Kinetics and mechanisms of hydrothermal synthesis of barium titanate. J Am Ceramic Soc 1996;79(11):2929–39. DOI: 10.1111/j.1151-2916.1996.tb08728.x

[61] Gao F, Chen XY, Yin KB, Dong S, Ren ZF, Yuan F, et al. Visible-light photocatalytic properties of weak magnetic $BiFeO_3$ nanoparticles. Adv Mater 2007;19(19):2889–92. DOI: 10.1002/adma.200602377

[62] Walton RI, Millange F, Smith RI, Hansen TC, O'Hare D. Real time observation of the hydrothermal crystallization of barium titanate using in situ neutron powder diffraction. J Am Chem Soc 2001;123(50):12547–55. DOI: 10.1021/ja011805p

[63] Komarneni S, Roy R, Li QH. Microwave-hydrothermal synthesis of ceramic powders. Mater Res Bull 1992;27(12):1393–405. DOI: 10.1016/0025-5408(92)90004-J

[64] A. Katsuki H, Komarneni S. Microwave-hydrothermal synthesis of monodispersed nanophase α-Fe_2O_3. J Am Ceramic Soc 2001;84(10):2313–7. DOI: 10.1111/j.1151-2916.2001.tb01007.x

[65] Komarneni S, Li Q, Stefansson KM, Roy R. Microwave-hydrothermal processing for synthesis of electroceramic powders. J Mater Res. 1993;8(12):3176–83. DOI: 10.1557/JMR.1993.3176

[66] Komarneni S, Li QH, Roy R. Microwave-hydrothermal processing for synthesis of layered and network phosphates. J Mater Chem 1994;4(12):1903–6. DOI: 10.1039/JM9940401903

[67] Komarneni S, Li QH, Roy R. Microwave-hydrothermal processing of layered anion exchangers. J Mater Res 1996;11(8):1866–9. DOI: 10.1557/JMR.1996.0236

[68] Liu S-F, Abothu IR, Komarneni S. Barium titanate ceramics prepared from conventional and microwave hydrothermal powders. Mater Lett 1999;38(5):344–350. DOI: 10.1016/S0167-577X(98)00187-6

[69] Jhung SH, Lee J-H, Yoon JW, Hwang YK, Hwang J-S, Park S-E, et al. Effects of reaction conditions in microwave synthesis of nanocrystalline barium titanate. Mater Lett 2004;58(25):3161–5. DOI: 10.1016/j.matlet.2004.06.006

[70] Sun W, Li C, Li J, Liu W. Microwave-hydrothermal synthesis of tetragonal $BaTiO_3$ under various conditions. Mater Chem Phys 2006;97(2–3):481–7. DOI: 10.1016/j.matchemphys.2005.08.051

[71] Pązik R, Hreniak D, Stręk W. Microwave driven hydrothermal synthesis of $Ba_{1-x}Sr_xTiO_3$ nanoparticles. Mater Res Bull 2007;42(7):1188–94. DOI: 10.1016/j.materresbull.2006.10.021

[72] Zhu X, Hang Q, Xing Z, Yang Y, Zhu J, Liu Z, et al. Microwave hydrothermal synthesis, structural characterization, and visible-light photocatalytic activities of single-crystalline bismuth ferric nanocrystals. J Am Ceramic Soc 2011;94(8):2688–93. DOI: 10.1111/j.1551-2916.2011.04430.x

[73] Zhu X, Yang Y, He K, Zhu J, Ye S, Zhou S, et al. Microwave-hydrothermal synthesis and structural characterization of multiferroic bismuth ferrite nanostructures. Ferroelectrics 2010;409(1):204–10. DOI: 10.1080/00150193.2010.486248

[74] Chen C, Cheng J, Yu S, Che L, Meng Z. Hydrothermal synthesis of perovskite bismuth ferrite crystallites. J Crystal Growth 2006;291(1):135–9. DOI: 10.1016/j.jcrysgro.2006.02.048

[75] Han JT, Huang YH, Wu XJ, Wu CL, Wei W, Peng B, et al. Tunable synthesis of bismuth ferrites with various morphologies. Adv Mater 2006;18(16):2145–8. DOI: 10.1002/adma.200600072

[76] Joshi UA, Jang JS, Borse PH, Lee JS. Microwave synthesis of single-crystalline perovskite $BiFeO_3$ nanocubes for photoelectrode and photocatalytic applications. Appl Phys Lett 2008;92(24):242106. DOI: 10.1063/1.2946486

[77] Li S, Lin Y-H, Zhang B-P, Wang Y, Nan C-W. Controlled fabrication of $BiFeO_3$ uniform microcrystals and their magnetic and photocatalytic behaviors. J Phys Chem C 2010;114(7):2903–8. DOI: 10.1021/jp910401u

[78] Hennings D, Schreinemacher S. Characterization of hydrothermal barium titanate. J Eur Ceramic Soc 1992;9(1):41–6. DOI: 10.1016/0955-2219(92)90075-O

[79] Nakano H, Urabe K, Oikawa T, Ikawa H. Characterization of internal pores in hydrothermally synthesized $BaTiO_3$ particle by transmission electron microscopy. J Am Ceramic Soc 2004;87(8):1594–7. DOI: 10.1111/j.1551-2916.2004.01594.x

[80] Sakabe Y. Grain size effect on dielectric properties and crystal structure of fine-grained $BaTiO_3$ ceramics. J Korean Phys Soc 1998;32:S260–4.

[81] Zhu X, Zhu J, Zhou S, Liu Z, Ming N. Hydrothermal synthesis of nanocrystalline $BaTiO_3$ particles and structural characterization by high-resolution transmission elec-

tron microscopy. J Crystal Growth 2008;310(2):434–41. DOI: 10.1016/j.jcrysgro.2007.10.076

[82] Wang ZL, Cowley JM. Simulating high-angle annular dark-field stem images including inelastic thermal diffuse scattering. Ultramicroscopy 1989;31(4):437–53. DOI: 10.1016/0304-3991(89)90340-9

[83] Pennycook SJ, Jesson DE. High-resolution incoherent imaging of crystals. Phys Rev Lett 1990;64(8):938–41. DOI: 10.1103/PhysRevLett.64.938

[84] Zhu X, Wang J, Zhang Z, Zhu J, Zhou S, Liu Z, et al. Atomic-scale characterization of barium titanate powders formed by the hydrothermal process. J Am Ceramic Soc 2008;91(3):1002–8. DOI: 10.1111/j.1551-2916.2007.02227.x

[85] Zhu X, Zhu J, Zhou S, Liu Z, Ming N, Hesse D. $BaTiO_3$ nanocrystals: hydrothermal synthesis and structural characterization. J Crystal Growth 2005;283(3–4):553–62. DOI: 10.1016/j.jcrysgro.2005.05.080

[86] Zhu X, Zhou J, Zhu J, Liu Z, Li Y, Al-Kassab T. Structural characterization and optical properties of perovskite $ZnZrO_3$ nanoparticles. J Am Ceramic Soc 2014;97(6):1987–92. DOI: 10.1111/jace.12883

[87] Hartman P, Perdok WG. On the relations between structure and morphology of crystals. I. Acta Crystallograph 1955;8(1):49–52. DOI: 10.1107/S0365110X55000121

[88] Jiang B, Peng JL, Bursill LA, Ren TL, Zhang PL, Zhong WL. Defect structure and physical properties of barium titanate ultra-fine particles. Phys B: Condens Matt 2000;291(1–2):203–12. DOI: 10.1016/S0921-4526(99)01874-8

[89] Jiang B, Peng JL, Bursill LA. Intergrowth defects and dielectric response of $BaTiO_3$ nano-particles. Ferroelectrics 1998;207(1):587–610. DOI: 10.1080/00150199808217271

[90] Rose H. Outline of a spherically corrected semiaplanatic medium-voltage transmission electron-microscope. Optik 1990;85(1):19–24.

[91] Urban KW. Studying atomic structures by aberration-corrected transmission electron microscopy. Science 2008;321(5888):506–10. DOI: 10.1126/science.1152800

[92] Jia C-L, Mi S-B, Urban K, Vrejoiu I, Alexe M, Hesse D. Atomic-scale study of electric dipoles near charged and uncharged domain walls in ferroelectric films. Nature Mater 2008;7(1):57–61. DOI: 10.1038/nmat2080

[93] Huang L, Chen Z, Wilson JD, Banerjee S, Robinson RD, Herman IP, et al. Barium titanate nanocrystals and nanocrystal thin films: synthesis, ferroelectricity, and dielectric properties. J Appl Phys 2006;100(3):034316. DOI: 10.1063/1.2218765

[94] Nuraje N, Su K, Haboosheh A, Samson J, Manning EP, Yang Nl, et al. Room temperature synthesis of ferroelectric barium titanate nanoparticles using peptide nanorings as templates. Adv Mater 2006;18(6):807–11. DOI: 10.1002/adma.200501340

[95] Markovic D, Kusigerski V, Tadic M, Blanusa J, Antisari MV, Spasojevic V. Magnetic properties of nanoparticle $La_{0.7}Ca_{0.3}MnO_3$ prepared by glycine–nitrate method without additional heat treatment. Scripta Materialia 2008;59(1):35–8. DOI: 10.1016/j.scriptamat.2008.02.020

[96] Moreira ML, Soares JM, de Azevedo WM, Rodrigues AR, Machado FLA, de Araújo JH. Structural and magnetic properties of nanoparticles of $La_{2/3}Sr_{1/3}MnO_3$. Phys B: Condens Matt 2006;384(1–2):51–3. DOI: 10.1016/j.physb.2006.05.044

[97] Uskoković V, Košak A, Drofenik M. Silica-coated lanthanum–strontium manganites for hyperthermia treatments. Mater Lett 2006;60(21–22):2620–2. DOI: 10.1016/j.matlet.2006.01.047

[98] Lipham ND, Tsoi GM, Wenger LE. Synthesis and characterization of Sr-doped lanthanum manganite nanoparticles. Magnetics, IEEE Transact 2007;43(6):3088–90. DOI: 10.1109/TMAG.2007.893850

[99] Park T-J, Papaefthymiou GC, Viescas AJ, Moodenbaugh AR, Wong SS. Size-dependent magnetic properties of single-crystalline multiferroic $BiFeO_3$ nanoparticles. Nano Lett 2007;7(3):766–72. DOI: 10.1021/nl063039w

[100] Selbach SM, Tybell T, Einarsrud M-A, Grande T. Size-dependent properties of multiferroic $BiFeO_3$ nanoparticles. Chem Mater 2007;19(26):6478–84. DOI: 10.1021/cm071827w

[101] Joshi PC, Desu SB. Structural, electrical, and optical studies on rapid thermally processed ferroelectric $BaTiO_3$ thin films prepared by metallo-organic solution deposition technique. Thin Solid Films 1997;300(1–2):289–94. DOI: 10.1016/S0040-6090(96)09468-0

[102] Cheong S-W, Mostovoy M. Multiferroics: a magnetic twist for ferroelectricity. Nat Mater 2007;6(1):13–20. DOI: 10.1038/nmat1804

[103] Rao CNR, Serrao CR. New routes to multiferroics. J Mater Chem 2007;17(47):4931–8. DOI: 10.1039/B709126E

[104] Zhao T, Scholl A, Zavaliche F, Lee K, Barry M, Doran A, et al. Electrical control of antiferromagnetic domains in multiferroic $BiFeO_3$ films at room temperature. Nat Mater 2006;5(10):823–9. DOI: 10.1038/nmat1731

[105] Chu Y-H, Martin LW, Holcomb MB, Gajek M, Han S-J, He Q, et al. Electric-field control of local ferromagnetism using a magnetoelectric multiferroic. Nat Mater 2008;7(6):478–82. DOI: 10.1038/nmat2184

[106] Fiebig M. Revival of the magnetoelectric effect. J Phys D: Appl Phys 2005;38(8):R123–52. DOI: 10.1088/0022-3727/38/8/R01

[107] Ederer C, Spaldin NA. Magnetoelectrics: a new route to magnetic ferroelectrics. Nat Mater 2004;3(12):849–51. DOI: 10.1038/nmat1265

[108] Yu J, Chu J. Progress and prospect for high temperature single-phased magnetic ferroelectrics. Chin Sci Bull 2008;53(14):2097–112. DOI: 10.1007/s11434-008-0308-3

[109] Setter N, Damjanovic D, Eng L, Fox G, Gevorgian S, Hong S, et al. Ferroelectric thin films: review of materials, properties, and applications. J Appl Phys 2006;100(5): 051606. DOI: 10.1063/1.2336999

[110] Kohlstedt H, Ishiwara H. Nanoelectronics and Information Technology - Advanced Electronic Materials and Novel Devices. 1st ed. Wienheim, Germany: WILEY-VCH Verlag; 2003. 1002 p.

[111] Martinelli G, Carotta MC, Traversa E, Ghiotti G. Thick-film gas sensors based on nano-sized semiconducting oxide powders. MRS Bull 1999;24(06):30–6. DOI: 10.1557/S0883769400052489

[112] Mathews S, Ramesh R, Venkatesan T, Benedetto J. Ferroelectric field effect transistor based on epitaxial perovskite heterostructures. Science 1997;276(5310):238–40. DOI: 10.1126/science.276.5310.238

[113] Tasch AF, Jr, Parker LH. Memory cell and technology issues for 64- and 256-Mbit one-transistor cell MOSD DRAMs. Proc IEEE 1989;77(3):374–88. DOI: 10.1109/5.24125

[114] Scott J. High-dielectric constant thin films for dynamic random access memories (DRAM). Annu Rev Mater Sci 1998;28(1):79–100. DOI: 10.1146/annurev.matsci.28.1.79

[115] Hwang CS, Park SO, Cho HJ, Kang CS, Kang HK, Lee SI, et al. Deposition of extremely thin (Ba, Sr) TiO_3 thin films for ultra-large-scale integrated dynamic random access memory application. Appl Phys Lett 1995;67(19):2819–21. DOI: 10.1063/1.114795

[116] Horikawa T, Mikami N, Makita T, Tanimura J, Kataoka M, Sato K et al. Dielectric properties of (Ba, Sr)TiO_3 thin films deposited by RF sputtering. Jpn J Appl Phys 1993;32(9S):4126–30. DOI: 10.1143/JJAP.32.4126

[117] Yoshino K, Shimoda Y, Kawagishi Y, Nakayama K, Ozaki M. Temperature tuning of the stop band in transmission spectra of liquid-crystal infiltrated synthetic opal as tunable photonic crystal. Appl Phys Lett 1999;75(7):932–4. DOI: 10.1063/1.124558

[118] Martí X, Sánchez F, Hrabovsky D, Fàbrega L, Ruyter A, Fontcuberta J, et al. Exchange biasing and electric polarization with $YMnO_3$. Appl Phys Lett 2006;89(3):032510. DOI: 10.1063/1.2234285

[119] Béa H, Bibes M, Cherifi S, Nolting F, Warot-Fonrose B, Fusil S, et al. Tunnel magnetoresistance and robust room temperature exchange bias with multiferroic $BiFeO_3$ epitaxial thin films. Appl Phys Lett 2006;89(24):242114. DOI: 10.1063/1.2402204

[120] Žutić I, Fabian J, Das Sarma S. Spintronics: fundamentals and applications. Rev Mod Phys 2004;76(2):323–410. DOI: 10.1103/RevModPhys.76.323

[121] Kimura T, Kawamoto S, Yamada I, Azuma M, Takano M, Tokura Y. Magnetocapacitance effect in multiferroic $BiMnO_3$. Phys Rev B 2003;67(18):180401. DOI: 10.1103/PhysRevB.67.180401

[122] Shaw TM, Trolier-McKinstry S, McIntyre PC. The properties of ferroelectric films at small dimensions. Ann Rev Mater Sci 2000;30(1):263–98. DOI: 10.1146/annurev.matsci.30.1.263

[123] Tsymbal EY, Kohlstedt H. Tunneling across a ferroelectric. Science 2006;313(5784):181–3. DOI: 10.1126/science.1126230

[124] Junquera J, Ghosez P. Critical thickness for ferroelectricity in perovskite ultrathin films. Nature 2003;422(6931):506–9. DOI: 10.1038/nature01501

[125] Pimenov A, Mukhin AA, Ivanov VY, Travkin VD, Balbashov AM, Loidl A. Possible evidence for electromagnons in multiferroic manganites. Nat Phys 2006;2(2):97–100. DOI: 10.1038/nphys212

[126] Eerenstein W, Mathur ND, Scott JF. Multiferroic and magnetoelectric materials. Nature 2006;442(7104):759–65. DOI: 10.1038/nature05023

IntechOpen